

Spatial Profiling of a Pd/Al₂O₃ Catalyst during Selective Ammonia Oxidation

Donato Decarolis,* Adam H. Clark, Tommaso Pellegrinelli, Maarten Nachtegaal, Evan W. Lynch, C. Richard A. Catlow, Emma K. Gibson, Alexandre Goguet,* and Peter P. Wells*



Cite This: *ACS Catal.* 2021, 11, 2141–2149



Read Online

ACCESS |



Metrics & More

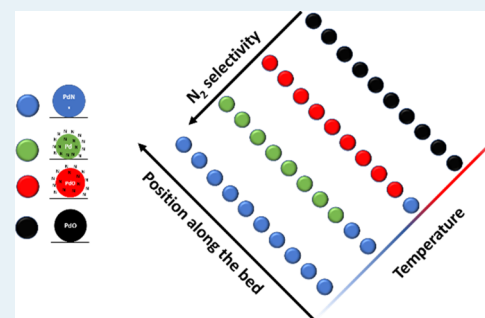


Article Recommendations



Supporting Information

ABSTRACT: The utilization of *operando* spectroscopy has allowed us to watch the dynamic nature of supported metal nanoparticles. However, the realization that subtle changes to environmental conditions affect the form of the catalyst necessitates that we assess the structure of the catalyst across the reactant/product gradient that exists across a fixed bed reactor. In this study, we have performed spatial profiling of a Pd/Al₂O₃ catalyst during NH₃ oxidation, simultaneously collecting mass spectrometry and X-ray absorption spectroscopy data at discrete axial positions along the length of the catalyst bed. The spatial analysis has provided unique insights into the structure–activity relationships that govern selective NH₃ oxidation—(i) our data is consistent with the presence of PdN_x after the spectroscopic signatures for bulk PdN_x disappear and that there is a direct correlation to the presence of this structure and the selectivity toward N₂; (ii) at high temperatures, ≥400 °C, we propose that there are two simultaneous reaction pathways—the oxidation of NH₃ to NO_x by PdO and the subsequent catalytic reduction of NO_x by NH₃ to produce N₂. The results in this study confirm the structural and catalytic diversity that exists during catalysis and the need for such an understanding if improvements to important emission control technologies, such as the selective catalytic oxidation of NH₃, are to be made.



KEYWORDS: ammonia oxidation, *operando* spectroscopy, Pd nanoparticles, SPACI-FB, heterogeneous catalysis

INTRODUCTION

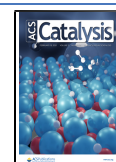
Advances in the design and optimization of heterogeneous catalysts for sustainable transformations and environmental protection require a precise understanding of structure–activity relationships. However, the structures of nanoparticle catalysts are extremely dynamic and are sensitive to fluctuations in the environmental conditions experienced during catalysis, e.g., along the path of a fixed bed reactor.^{1–3} A good example of this intricate structural selectivity has recently been established for the selective catalytic oxidation of NH₃ (NH₃-SCO).⁴ Ammonia selective catalytic reduction (SCR) is a necessary technology for the abatement of NO_x compounds from automotive exhausts.⁵ However, the process often leads to unwanted ammonia slip and the current legislation within the EU limits the emissions of this harmful gas to <10 ppm. Consequently, a NH₃-SCO catalyst is needed downstream of the deNO_x process to convert any unreacted NH₃ to N₂.⁶ The catalyst must be capable of achieving the complete conversion of NH₃ to N₂ without overoxidation to NO_x. Both transition (e.g., Cu,^{7,8} Fe^{9–12}) and noble (Pt,¹³ Ru,¹⁴ Pd,^{4,11,15} Rh¹⁶) metal catalysts have been assessed for their properties toward ammonia oxidation. Transition metals have shown strong selectivity to N₂, but at the required working temperature (<300 °C), the activity is not sufficient for their implementation in commercial applications.⁶ Con-

versely, noble metals are both active and selective at these temperatures and offer a viable solution. There still remains a challenge with noble metal catalysts—mitigating the over-oxidation of ammonia to further NO_x products. For example, Pt is among the most active of catalysts for ammonia oxidation; however, its selectivity to N₂ is low (36% at 300 °C).¹³ Other noble metal catalysts have been tested and among which, some of the most promising are Pd-based catalysts. Supported Pd nanoparticles (NPs) achieve good selectivity toward N₂, although there is a strong temperature dependence on the product distribution. In our recent work, we reported on a unique structural selectivity during the NH₃-SCO.⁴ Under reaction conditions, Pd incorporates nitrogen as a heteroatom at an interstitial site within the FCC structure, forming PdN_x. PdN_x was found as the dominant species during N₂ formation. At higher temperatures, both surface and bulk Pd oxides are produced, which drive the reaction toward NO_x products. These results showed that different phases were formed during

Received: December 7, 2020

Revised: January 8, 2021

Published: February 3, 2021



the reaction process, each affecting the selectivity of the catalyst. However, since concentration and temperature gradients are present along a plug-flow reactor, different phases may be present at different positions along the bed.³ The commonly employed single-point spectroscopy measurements might therefore miss much-sought insight on the reaction process. The inclusion of a spatial component is necessary to fully understand how a catalyst interacts with the gases in a plug-flow reactor. In many cases, this involves coupling a fixed bed reactor with a spectroscopic technique, e.g., UV/vis,^{17,18} FTIR,^{2,19} Raman,^{20,21} and XAFS.^{22,23} For example, Doronkin et al. utilized a fixed bed reactor coupled with spatially resolved *operando* XAFS studies to probe zeolite catalysts for the selective catalytic oxidation of NO_x by NH₃.¹ They demonstrated the presence of different catalyst zones, whose position and composition changes as a function of reaction temperature and gas flow characteristics. Furthermore, some recent studies are able to combine spatially resolved spectroscopic methods simultaneously, for example, Dann et al. were able to follow the kinetic oscillations experienced during CO oxidation using combined XAFS/DRIFTS over Pd/Al₂O₃ and found a strong spatial dependence on the nature of the oscillations.²⁴ Elsewhere, other groups have tackled this challenge by measuring the local gas composition using spatially resolved mass spectrometry, for example, Russell et al. were able to resolve the effect of thermal degradation of Pt/Al₂O₃ monolith-supported catalysts for the propylene oxidation reaction.²⁵

In the present study, we have utilized a method that merges these approaches, i.e., Spaci-FB-XAFS,³ a minimally invasive technique that allows monitoring of the gas-phase concentrations as well as the temperatures along a reactor bed (Spaci-FB),^{26,27} with X-ray absorption fine structure (XAFS) spectroscopy,³ which provides information on the local Pd speciation. Using this methodology, it was possible to profile the catalyst properties along a fixed catalytic bed and obtain both chemical and structural information on the Pd speciation in NH₃-SCO.

■ EXPERIMENTAL SECTION

Sample Preparation. A 1.5 wt % Pd/ γ -Al₂O₃ catalyst was prepared by incipient wetness impregnation of an acidified aqueous solution of palladium nitrate (15.11 wt % Pd, Johnson Matthey) onto a γ -Al₂O₃ (Sasol, 140 m² g⁻¹) at room temperature. The sample was subsequently dried at 100 °C and calcined in air at 500 °C for 2 h. The Pd/Al₂O₃ catalyst used in this study has been thoroughly characterized with the structural information reported elsewhere.⁴

SPACI-FB-XAS Measurement. The XAS measurements were performed at the Swiss Light Source (SLS) on the SuperXAS beamline,²⁸ around the Pd K edge (24.35 keV, by means of Si(311) crystal) in transmission mode with 15 cm long ion chambers filled with 1 bar N₂ and 1 bar Ar. The catalyst (200 mg), in a 150–250 μ m sieve fraction, was loaded in a quartz reactor (\varnothing 4 mm), resulting in a bed length of 10 mm. The quartz reactor was then loaded into the Spaci-FB system, and the gas sampling apertures, the thermocouple, and the X-ray beam (focused to a spot size of 250 \times 250 μ m by a Pt-coated toroidal mirror) were aligned to ensure that coincident measurements were conducted at the same axial point in the catalyst bed. The effluent gas composition was simultaneously measured using a mass spectrometer (MS). More details about the Spaci-FB setup are available else-

where.^{3,26} The experiment procedure consisted of the following: (1) reduction of the catalyst at 400 °C using 5% H₂ in He (40 mL min⁻¹); (2) cooling down to 100 °C under He and XAFS spectra collection along the axial direction of the bed at 11 discrete positions; (3) admission of the reactant mixture (0.5% NH₃, 2.5% O₂, and 97% He) at 100 °C; (4) after steady state has been reached, XAFS spectra collection, gas composition analysis, and temperature measurement were performed at 11 discrete axial positions, with position 0 being the inlet. The system reached steady state \sim 30 min after the introduction of the reactants, which was checked by measuring the MS response at the end of the reactor bed. The same procedure was employed after raising the temperature to 175, 300, and 400 °C. For each axial position, XAFS spectra were collected for 10 min, for a total of 1197 spectra. The XAFS data was processed using ProQEXAFS software²⁹ from the beamline to obtain a 10 min averaged spectrum for each point. The composition of effluent gas was measured using a mass spectrometer (Hiden QGA) for H₂ (m/z = 2), He (m/z = 4), NH₃ (m/z = 17), H₂O (m/z = 18), N₂ (m/z = 28), NO (m/z = 30), O₂ (m/z = 32), N₂O (m/z = 44), and NO₂ (m/z = 46).

XAFS Data Fit. The merged spectra were analyzed using Athena and Artemis from the Demeter IFEFFIT package.^{30,31} The FEFF6 code was used to construct theoretical EXAFS signals that included single-scattering contributions from atomic shells through the nearest neighbors, using O, N, and Pd as scatterers. The fit was performed using a k -range between 3 and 10.9 Å⁻¹ and an R range between 1 and 3.5 Å. The amplitude reduction factor (S_0^2) was fixed at 0.74, as obtained from fitting the bulk Pd foil reference. For temperature >300 °C the Debye–Waller factor was fixed to 0.03 for both the Pd–PdO and Pd–O scattering shells due to the high correlation with the coordination number and to reduce the number of independent parameters.

Multivariate Component Analysis. Multivariate curve resolution (MCR) was used to identify the various phases present in the sample through the analysis of its principal components.^{32–34} Here, regularly linear combination fitting of the XANES region of XAS spectra is undertaken from representative reference compounds, in cases where transient species or those that are not well reflected by stable reference compounds MCR methods provide an alternative approach to understand complex speciation problems.^{32,35,36} The linear combination of pure spectral components retrieved from MCR analysis can be used to describe the condition-dependent speciation during a time-resolved *operando* XAS experiment

$$\mu_{\text{exp}}(t, E) = \sum_i^{N_{\text{pure}}} \omega_i^{\text{pure}}(t) \times \mu_i^{\text{pure}}(E)$$

where the experimental spectrum, μ_{exp} , is described as the sum of the product of the weighted component fractions, ω_i^{pure} , and the resolved pure spectral components, μ_i^{pure} . As such the decomposition of a data matrix $D(m \times n)$ of m rows and n columns into matrices of the pure components of the k present species and the condition evolving concentration profiles $C(m \times k)$ and $S^T(k \times n)$ ³⁷

$$D = CS^T + E$$

here, the residual of the linear combination is explicitly given by matrix E . Where linear combination analysis involves only the least-squares refinement of the component concentrations, MCR analysis involves the iterative least-squares refinement of

both the concentration and spectral profiles. Using such an approach allows resolving the spectral signatures of the pure components that describe the changing data matrix supplied. Here, the initial guess of the pure spectral components was undertaken using the purest variable approach proposed by Windig et al.³⁸ However, one should be aware that the MCR methods are unable to readily separate coevolving components and thus the total number of MCR-modeled species may be lower than the actual number of species present. Further to this, non-negativity constraints were applied to both the spectral and concentration profiles and that the component concentration sum to unity during the MCR analysis. The analysis was performed using MCR-ALS developed by Tauler et al.³⁹

RESULTS

The combined SPACI-FB-XAS measurements during NH_3 -SCO over the $\text{Pd}/\text{Al}_2\text{O}_3$ provide information on the catalyst activity (from the MS data) as well as the change in the catalyst structure (through XAFS) at discrete positions within the catalyst bed.²⁶ The $\text{Pd}/\text{Al}_2\text{O}_3$ catalyst used in this study has been thoroughly characterized with the structural information reported elsewhere.⁴ Prior to performing NH_3 oxidation, the catalyst was loaded into the Spaci-FB reactor and treated in H_2 at 400 °C before cooling down under He. The XANES analysis of the catalyst after the prereduction treatment for the axial position, 0 (at the reactor inlet), is reported in Figure 1 and is consistent with nanoparticulate Pd^0 .^{40–42} The EXAFS analysis (Figure S1, Table S1)⁴³ was used to determine an average particle size of 1.9 nm.⁴³

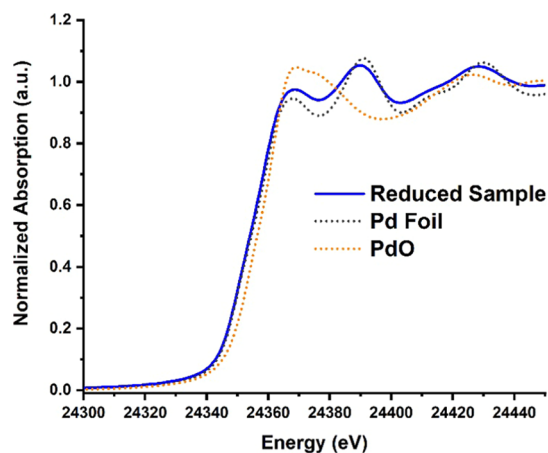


Figure 1. XANES spectra of $\text{Pd}/\text{Al}_2\text{O}_3$ after reduction, at axial position 0 within the bed compared to Pd foil and PdO reference.

The reactant mixture consisting of NH_3 , O_2 , and He was then introduced to the SPACI-FB-XAS reactor at 100 °C (Figure 2), before the onset of NH_3 oxidation.

Figure 2 confirms that a predominant interstitial PdN_x structure had formed uniformly across the catalyst bed prior to NH_3 oxidation, with the possible presence of an oxide layer on the surface of the catalyst. The formation of PdN_x was shown (Figure 2a; positions 1 and 8) by the higher intensity of the whitenline at 24 368 eV and the shift of the multiple scattering peaks at 24 390 and 24 420 eV toward lower energy compared to the Pd foil. To assess changes to the PdN_x phase as a function of axial position (Figure 2b), we chose to look at the intensity of the normalized XANES at 24 368 and 24 388

eV; 24 368 eV is the “whitenline” maximum and is sensitive to changes to the oxidic/metallic fraction; 24 388 eV is a position in the XANES profile where PdN_x has a greater intensity than both metallic and oxidic forms. Within the errors of the measurement, there is no statistically relevant variance in the intensities of these features. Furthermore, the Pd–Pd and Pd–N/O coordination numbers (Figure 2c) obtained from the fit (Figure S3, Table S2) are consistent across the catalyst profile, as is the expanded Pd–Pd distance of 2.81 Å (Figure 2d, Table S2) compared to standard 2.74 Å of metallic Pd. All data confirms a homogeneous level of PdN_x formation across the catalyst bed.

To enhance the information obtainable from the XANES region, multivariate curve resolution (MCR) analysis was employed using the full series of measurements at the different temperatures in this study to extract discrete principal components. MCR methods are particularly powerful in separating and identifying the evolving species within a large data set. Here, MCR methods are able to provide new insight by resolving the spectral signatures of three principal components (Figure 3a), which can be attributed to oxidic Pd (PdO MCR), metallic Pd (Pd^0 MCR), and PdN_x (PdN_x MCR). When applying this analysis to the data under reaction conditions at 100 °C, it is clear that PdN_x is the major phase present, as we have already identified. However, we are also able to identify a minor amount of both PdO MCR and Pd^0 MCR components (Figure 3b). Again, the proportion of these phases is consistent across the spatial profile of the catalyst bed.

At 175 °C (Figure 4), prior to full conversion of NH_3 , there is a clear spatial variance of the Pd speciation along the bed. From both the XANES (Figure 4a,b) and the EXAFS (Figures 4c and S5, Table S3), the sample is consistent with PdN_x for the first 2 mm of the bed. At increased axial positions, the multiple scattering features at 24 390 and 24 420 eV shift toward higher energy, indicative of heteroatom removal from the interstitial sites and an increase in metallic character, also confirmed by the shift of the bond length from ~ 2.8 Å to that of metallic Pd at 2.74 Å. Elsewhere, the change in Pd–Pd coordination number to lower values from 3 mm onwards and the consistent Pd–N/O coordination number are indicative of a partial oxidation after the bulk nitride structure is disrupted. However, the normalized intensity of the position at 24 388 eV does not decrease to the levels expected of either metallic or oxidic Pd, confirming that some Pd nitride remains.

When assessing the structural changes using MCR analysis, a similar picture emerges (Figure 4b); the nitride is dominant at the start of the bed ($\sim 60\%$) but decreases at higher axial positions ($\sim 30\%$), which is concomitant with an increase in Pd^0 MCR ($\sim 50\%$) and PdO MCR ($\sim 20\%$) components. This change is also manifested in the Pd–Pd distance, decreasing from 2.79 to 2.73 Å. A Pd–Pd distance of 2.73 Å is consistent with metallic Pd–Pd with negligible lattice expansion, as a consequence of heteroatom inclusion (Figure S5). However, there is still a significant XANES signature consistent with PdN_x . These structural changes can be interpreted as a replacement of a bulk PdN_x structure by one in which nitrogen is predominantly at the surface of the Pd NP. Indeed, work on the carbide forms of Pd have also reported that there is XANES signature consistent with Pd carbide in the absence of Pd–Pd lattice expansion that was also ascribed to surface species.⁴⁴ This hypothesis is also consistent with previous studies on Pd boride,⁴⁵ where authors have found that a

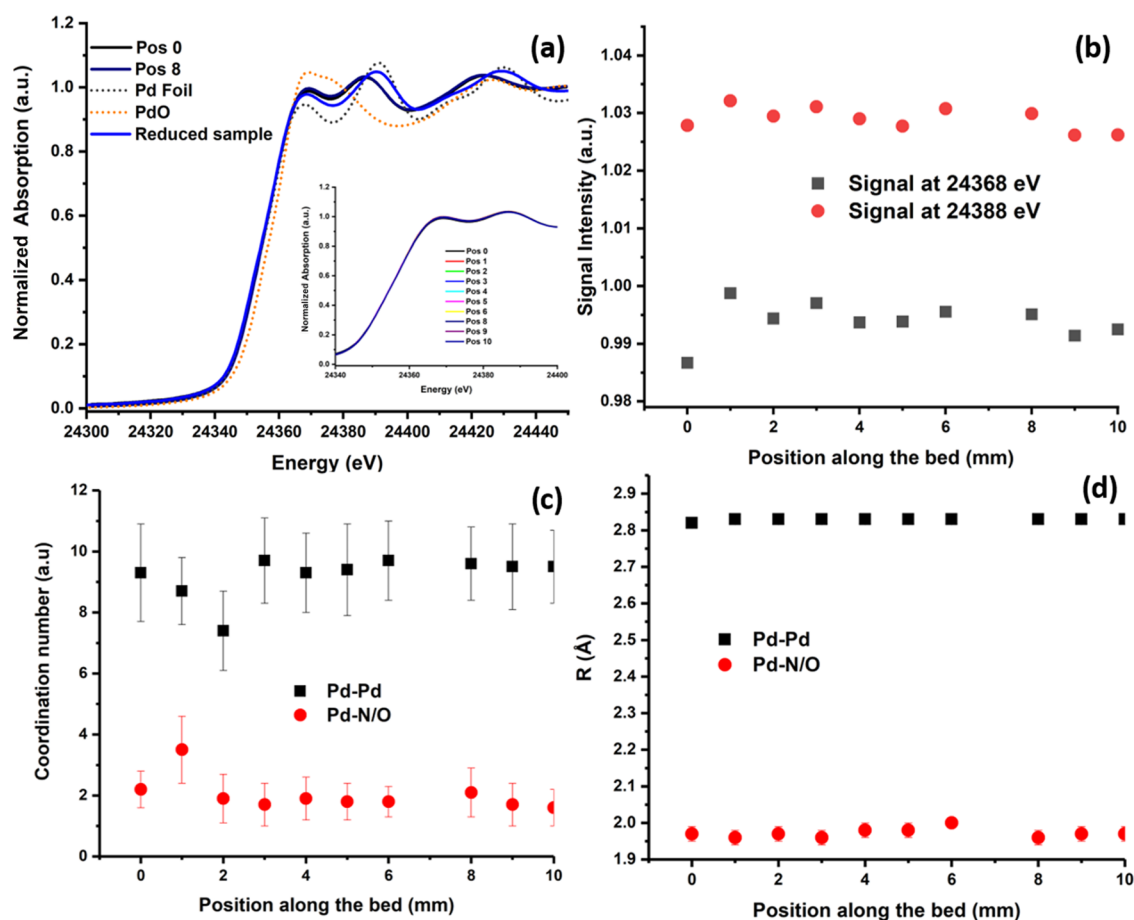


Figure 2. Pd/Al₂O₃ at 100 °C under reaction conditions. (a) XANES spectra of Pd/Al₂O₃ under reaction condition, 100 °C, for the front and the end of the bed, compared to Pd foil and PdO reference; (b) intensity of XANES at the whiteline (24 368 eV) and at the PdN_x peak (24 388 eV) along the catalyst bed; (c) Pd–Pd and Pd–N coordination number obtained from EXAFS fit; and (d) Pd–Pd and Pd–N/O distances obtained from EXAFS fit (the error is present but smaller than the symbol size). Mass spectrometry data can be found in Figure S2.

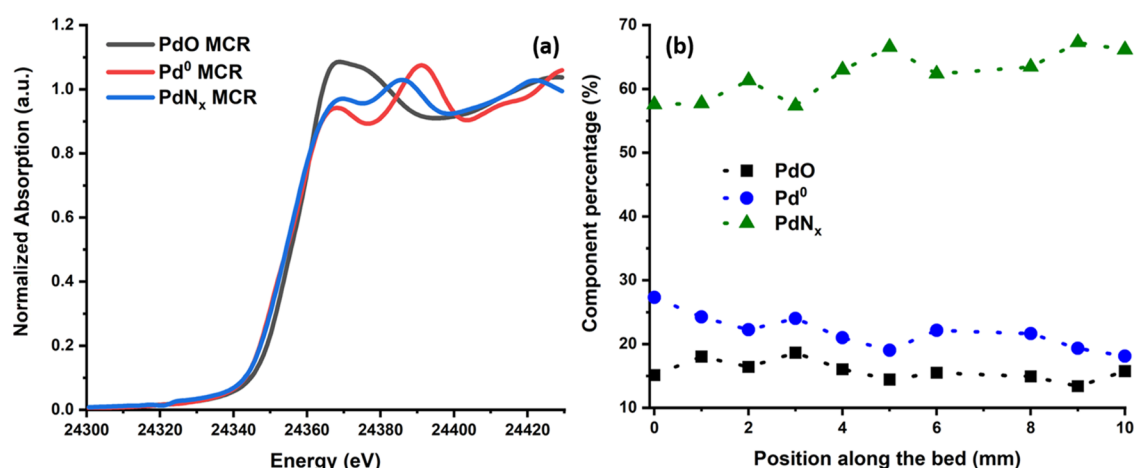


Figure 3. (a) MCR of the identified spectral components: oxidic Pd, PdO (black), metallic Pd⁰ (red), and PdN_x (blue). See Figure S4 for a comparison with reference spectra (b) spatial profile of the component percentage for Pd/Al₂O₃ under reaction conditions, 100 °C.

decomposition process takes place at higher temperature due to a phase separation induced by the oxygen. At this point, we cannot rule out the possibility that some interstitial nitride resides in the interior of the particle; however, considering the Pd–Pd distance observed, it would be anticipated that this only a minor contribution. The other unresolved question is the spatial relationship of the oxide and nitride species, which

still requires further investigation. Notwithstanding, the identification of this nitride signature is an important insight, as previously we had only identified the bulk nitride structure. The spatial analysis and the use of MCR have been crucial in providing this additional information.

The SPACI-FB-XAS approach has identified two areas that need further clarification: (i) what drives the change in PdN_x

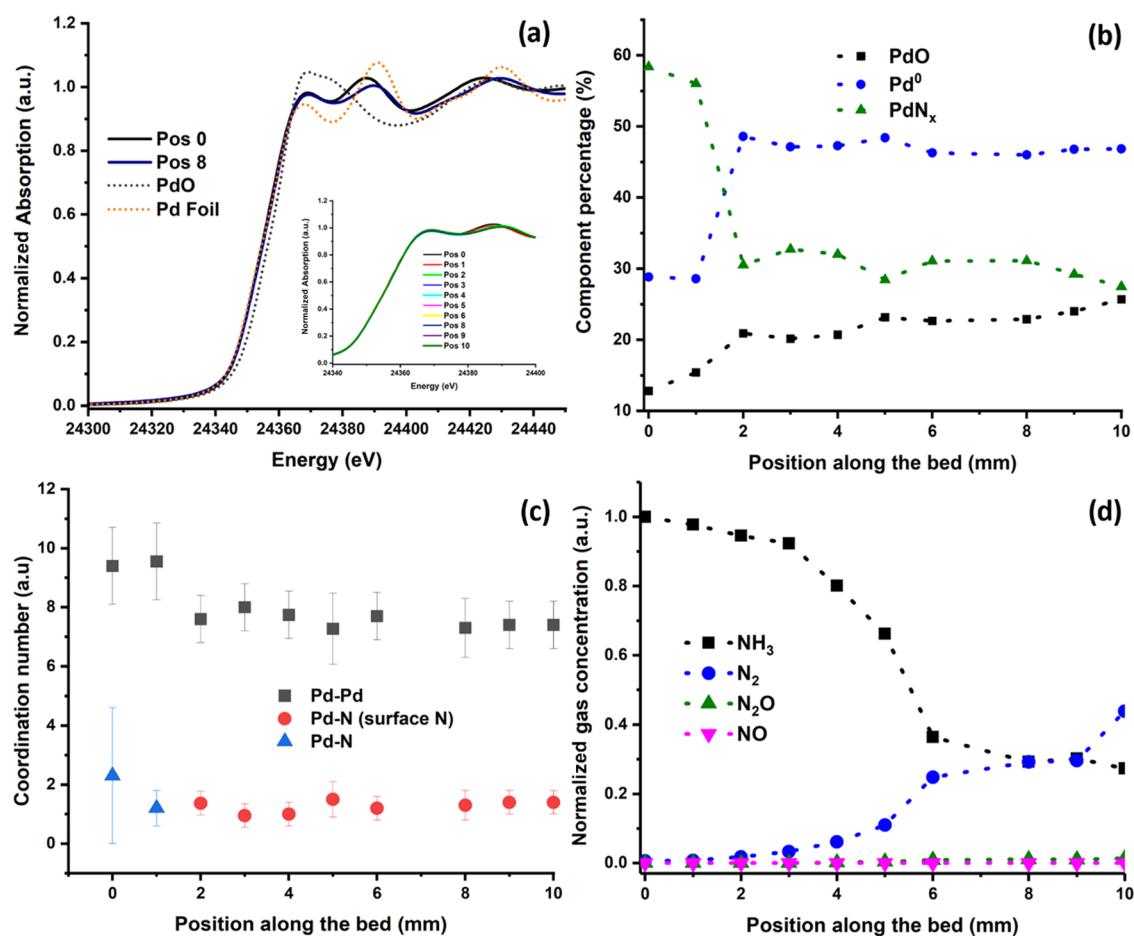


Figure 4. Pd/Al₂O₃ at 175 °C. (a) XANES spectra of Pd/Al₂O₃ under reaction condition, 175 °C, for the front and the end of the bed, compared to Pd foil and PdO reference; (b) component percentage, obtained from MCR, for Pd/Al₂O₃ under reaction conditions, 175 °C, at various positions along the bed; (c) Pd–Pd, Pd–N, and Pd–N/O coordination number obtained from EXAFS fit; and (d) normalized mass spectrometry signal along the bed; the intensity of XANES at the whitenline (24 368 eV) and at the PdN_x peak (24 388 eV) along the catalyst bed is shown in Figure S6.

structure at 2 mm from the inlet of the reactor and (ii) how is this structural change linked with the “light-off” for NH₃ conversion?

The answers to both points are linked: NH₃ oxidation is an exothermic process and our temperature profiles measured across the bed (Figure S7) illustrate an increase in temperature from inlet to outlet. It is worth noting that this recorded temperature represents the macroscopic temperature within the reactor and does not reflect the temperature at the surface of individual particles, which is likely to be significantly higher. At the front of the bed, before the onset of significant NH₃ oxidation, the catalyst is at a lower temperature and the Pd remains predominantly PdN_x. As the exotherm linked to NH₃ oxidation propagates, the temperature increase allows the bulk interstitial nitrogen to become mobile, and there is a reduction in nitride character and an observable increase in NH₃ conversion and N₂ production (Figure 4d). However, the XANES MCR analysis confirms that there is still significant PdN_x on the surface of Pd NPs. Eventually, the exotherm raises the temperature enough to cause the sharp light-off for NH₃ conversion.

As the concentration of NH₃ decreases, there is a concomitant drop off in the rate of reaction and a plateau in the NH₃ conversion; the reaction is not zero order with respect

to [NH₃], and the conversion of NH₃ is dependent upon its concentration.

An analogous experiment was performed at 300 °C (Figure 5)—the temperature at which higher oxidation products, e.g., N₂O, first appear. The initial inlet of the reactor (axial position 0) is predominantly PdN_x as shown by the XANES (Figure 5a,b) and EXAFS (Figures 5c and S8, Table S4) spectra. However, by the second position in the bed (axial position 1), there is a profound structural change. There is a sharp increase in the intensity of the XANES main edge transition at 24 368 eV (Figure 5a), and the EXAFS is dominated by the primary shell coordination to oxygen (Figure 5c). It is clear that Pd NPs have started the process of forming a bulk PdO phase. The EXAFS data show a contribution of a distinct oxide Pd–Pd scattering distance, with, however, a relatively small coordination number.

The catalytic activity (Figure 5d) shows a sharp and sustained decrease in NH₃ concentration between axial positions 0 and 6. However, despite the large extent of oxide coverage on the surface, there is still a strong selectivity toward N₂. The XANES MCR (Figure 5b) analysis demonstrates that despite the strong oxide signatures, through visually inspecting the XANES and EXAFS, there is ~ a 20% content of PdN_x from axial position 1 onwards. It is increasingly apparent that the selectivity to N₂ is influenced by the residual Pd nitride

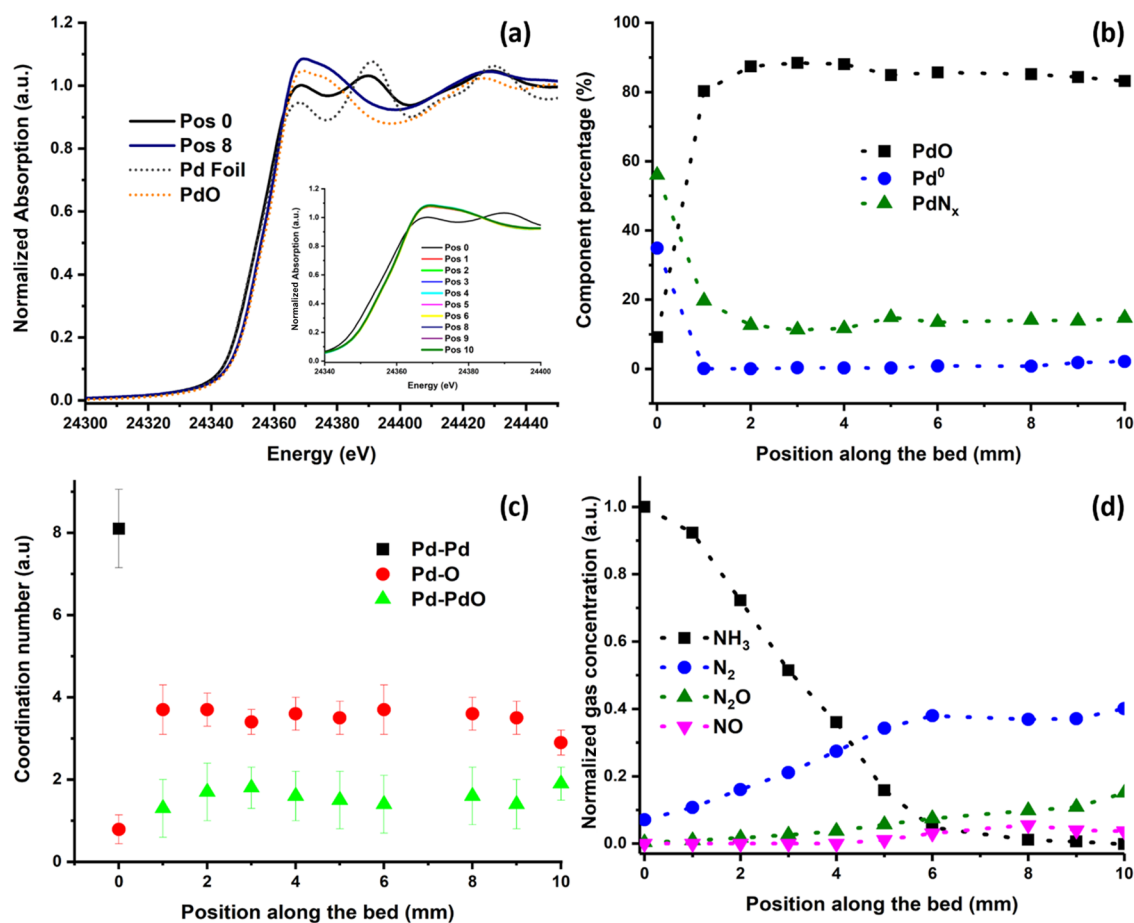


Figure 5. Spatial analysis of Pd/Al₂O₃ at 300 °C under reaction conditions. (a) XANES spectra; (b) component percentage, obtained from MCR, for Pd/Al₂O₃ under reaction conditions, 300 °C, at various positions along the bed. (c) Pd–Pd, Pd–N/O, Pd–O (in PdO), and Pd–PdO coordination number obtained from EXAFS fit; and (d) Pd–Pd normalized mass spectrometry signal along the bed; the intensity of XANES at the whiteline (24 368 eV) and at the PdN_x peak (24 388 eV) along the catalyst bed is shown in Figure S9.

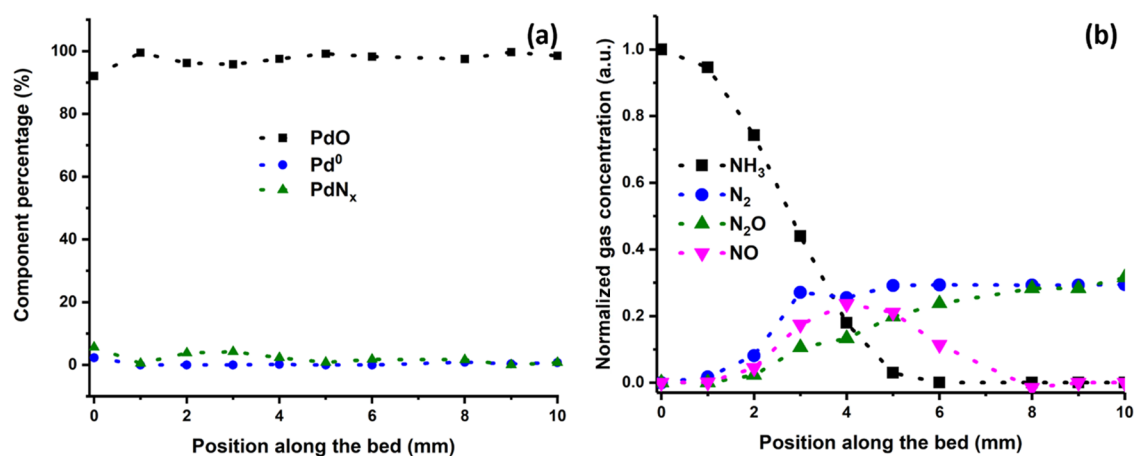


Figure 6. (a) Component percentage, obtained from MCR, for Pd/Al₂O₃ under reaction conditions, 400 °C, at various positions along the bed; (b) normalized mass spectrometry signal along the bed.

even in the presence of significant amounts of oxidic Pd that drive the production to further oxygenated products.

When the temperature was increased further to 400 °C (Figure 6), an entirely different catalytic behavior was observed. As the bed is traversed from inlet to outlet, there are increases to N₂, N₂O, and NO until position 4, at which point the level of NO decreases, which is accompanied by a

halt in the production of N₂. This suggests a shift in the selectivity of the catalyst. Observing the MCR data, it is possible to see that there is still a minimal amount of PdN_x present (~5%) up until position 4, which is then completely consumed. It can be therefore inferred that, at least in the first part of the bed, a catalytic oxidation of NH₃ is taking place, albeit with its selectivity toward N₂ severely impacted by the

lack of a suitable amount of PdN_x. However, these findings pose an important question: why does the NO level rise and fall across the length of the catalyst bed? There could be another set of reactions taking place once the PdN_x phase is removed: a reaction of NO with NH₃ to produce N₂O and the oxidation of NO to form NO₂, with a further reaction of NO₂ with NH₃ to form N₂O, in a SCR-like behavior. This reaction has already been studied on Pd nanoparticulate species using H₂^{46,47} or methane^{48,49} as a reducing agent. To the best of our knowledge, no study has been reported on the capability of Pd to reduce NO_x selectively in the presence of ammonia; from the studies that have been performed, it is entirely plausible that this reaction is possible on Pd, even if to a limited extent. Whereas the presence of NO₂ could not be ascertained, as no changes in the *m/z* = 46 response could be observed, it is possible to observe a steady increase in the N₂O production across the bed. From position 4 onwards, we propose: (i) the catalyst undergoes a shift in selectivity, likely caused by the removal of the PdN_x phase; (ii) N₂ and NO production stops and NO is progressively consumed to form either NO₂ and/or N₂O.

CONCLUSIONS

This study further demonstrates the intricate complexity of heterogeneous catalysis. Studying the spatial variance of gas composition and catalyst speciation at a series of isothermal conditions during NH₃-SCO on Pd/Al₂O₃ has provided additional insights. During the temperature series <400 °C, we have established:

- That at the inlet of the reactor the Pd speciation is predominantly PdN_x.
- As the reaction exotherm progresses toward the outlet of the reactor, the bulk interstitial N becomes mobile.
- The MCR analysis identifies a nitride phase present, even though the Pd–Pd distance is indicative that it is absent from the bulk of the particle. This finding is consistent with the presence of a surface nitride structure.
- While the nitride is present, there is still appreciable selectivity toward N₂. As the particle becomes increasingly oxidized, there is a change in selectivity toward undesirable NO_x products.

Moreover, at 400 °C, our data are no longer exclusively consistent with NH₃-SCO and can be rationalized by an additional reaction pathway of NH₃-SCR-like; the NH₃-SCO process yields NO_x products, which are reduced by residual NH₃. There is direct evidence of this process, as the spatial analysis identifies the consumption of NO, to produce additional amounts of N₂O.

This study has not only provided crucial insights into NH₃-SCO over Pd/Al₂O₃ but it also further demonstrates that *in situ* and *operando* analysis that relies on single-point analysis can miss vitally important information. The need for full spatial analysis is increasingly apparent and will take on additional importance as more studies, as is described here, are reported.

ASSOCIATED CONTENT

Supporting Information

The Supporting Information is available free of charge at <https://pubs.acs.org/doi/10.1021/acscatal.0c05356>.

EXAFS fit results, MCR results, XANES whitenline analysis, and reactor temperature (PDF)

AUTHOR INFORMATION

Corresponding Authors

Donato Decarolis — Cardiff Catalysis Institute, School of Chemistry, Cardiff University, Cardiff CF10 3AT, U.K.; UK Catalysis Hub, Research Complex at Harwell, Rutherford Appleton Lab, Harwell, Oxfordshire OX11 0FA, U.K.; Email: decarolisd@cardiff.ac.uk

Alexandre Goguet — School of Chemistry, Queen's University Belfast, Belfast BT9 5AG, U.K.; UK Catalysis Hub, Research Complex at Harwell, Rutherford Appleton Lab, Harwell, Oxfordshire OX11 0FA, U.K.; Email: a.goguet@qub.ac.uk

Peter P. Wells — UK Catalysis Hub, Research Complex at Harwell, Rutherford Appleton Lab, Harwell, Oxfordshire OX11 0FA, U.K.; School of Chemistry, University of Southampton, Southampton SO17 1BJ, U.K.; Diamond Light Source Ltd., Didcot OX11 0DE, U.K.; orcid.org/0000-0002-0859-9172; Email: P.P.Wells@soton.ac.uk

Authors

Adam H. Clark — Paul Scherrer Institute, 5232 Villigen PSI, Switzerland; orcid.org/0000-0002-5478-9639

Tommaso Pelleggrinelli — School of Chemistry, Queen's University Belfast, Belfast BT9 5AG, U.K.

Maarten Nachtegaal — Paul Scherrer Institute, 5232 Villigen PSI, Switzerland; orcid.org/0000-0003-1895-9626

Evan W. Lynch — School of Chemistry, University of Southampton, Southampton SO17 1BJ, U.K.; UK Catalysis Hub, Research Complex at Harwell, Rutherford Appleton Lab, Harwell, Oxfordshire OX11 0FA, U.K.

C. Richard A. Catlow — Cardiff Catalysis Institute, School of Chemistry, Cardiff University, Cardiff CF10 3AT, U.K.; UK Catalysis Hub, Research Complex at Harwell, Rutherford Appleton Lab, Harwell, Oxfordshire OX11 0FA, U.K.; Department of Chemistry, University College London, London WC1 HOAJ, U.K.; orcid.org/0000-0002-1341-1541

Emma K. Gibson — School of Chemistry, University of Glasgow, Glasgow G12 8QQ, U.K.; UK Catalysis Hub, Research Complex at Harwell, Rutherford Appleton Lab, Harwell, Oxfordshire OX11 0FA, U.K.; orcid.org/0000-0002-7839-3786

Complete contact information is available at:

<https://pubs.acs.org/doi/10.1021/acscatal.0c05356>

Author Contributions

The manuscript was written through the contributions of all authors. All authors have given approval to the final version of the manuscript.

Notes

The authors declare no competing financial interest.

All data supporting this study are openly available from the University of Southampton repository at <https://doi.org/10.5258/SOTON/D1723>.

ACKNOWLEDGMENTS

The authors acknowledge the Swiss Light Source for the provision of beamtime at SuperXAS. Queen's University Belfast is acknowledged for the use of their facilities. The RCaH is acknowledged for the use of facilities and staff support. UK Catalysis Hub is kindly thanked for resources and support provided via our membership of the UK Catalysis Hub Consortium and funded by EPSRC grant: EP/R026939/1,

EP/R026815/1, EP/R026645/1, EP/R027129/1, or EP/M013219/1 (biocatalysis).

REFERENCES

- (1) Doronkin, D. E.; Casapu, M.; Günter, T.; Müller, O.; Frahm, R.; Grunwaldt, J.-D. Operando Spatially- and Time-Resolved XAS Study on Zeolite Catalysts for Selective Catalytic Reduction of NO_x by NH₃. *J. Phys. Chem. C* **2014**, *118*, 10204–10212.
- (2) Daniel, C.; Clarté, M.-O.; Teh, S.-P.; Thinon, O.; Provendier, H.; Van Veen, A. C.; Beccard, B. J.; Schuurman, Y.; Mirodatos, C. Spatially Resolved Catalysis in Microstructured Reactors by IR Spectroscopy: CO Oxidation over Mono- and Bifunctional Pt Catalysts. *J. Catal.* **2010**, *272*, 55–64.
- (3) Stewart, C.; Gibson, E. K.; Morgan, K.; Cibir, G.; Dent, A. J.; Hardacre, C.; Kondratenko, E. V.; Kondratenko, V. A.; McManus, C.; Rogers, S.; Stere, C. E.; Chansai, S.; Wang, Y.-C.; Haigh, S. J.; Wells, P. P.; Goguet, A. Unraveling the H₂ Promotional Effect on Palladium-Catalyzed CO Oxidation Using a Combination of Temporally and Spatially Resolved Investigations. *ACS Catal.* **2018**, *8*, 8255–8262.
- (4) Dann, E. K.; Gibson, E. K.; Blackmore, R. H.; Catlow, C. R. A.; Collier, P.; Chutia, A.; Erden, T. E.; Hardacre, C.; Kroner, A.; Nachtegaal, M.; Raj, A.; Rogers, S. M.; Taylor, S. F. R.; Thompson, P.; Tierney, G. F.; Zeinalipour-Yazdi, C. D.; Goguet, A.; Wells, P. P. Structural Selectivity of Supported Pd Nanoparticles for Catalytic NH₃ Oxidation Resolved Using Combined Operando Spectroscopy. *Nat. Catal.* **2019**, *2*, 157–163.
- (5) Bull, I.; Xue, W.; Burk, P.; Boorse, R. S.; Jaglowski, W. M.; Koermer, G. S.; Moini, A.; Patchett, J. A.; Dettling, J. C.; Claude, M. T.U.S. Patent US7,601,662B2, 2009.
- (6) Chmielarz, L.; Jabłońska, M. Advances in Selective Catalytic Oxidation of Ammonia to Dinitrogen: A Review. *RSC Adv.* **2015**, *5*, 43408–43431.
- (7) Zhang, X.; Wang, H.; Wang, Z.; Qu, Z. Adsorption and Surface Reaction Pathway of NH₃ Selective Catalytic Oxidation over Different Cu-Ce-Zr Catalysts. *Appl. Surf. Sci.* **2018**, *447*, 40–48.
- (8) Wang, D.; Zhang, L.; Kamasamudram, K.; Epling, W. S. In Situ DRIFTS Study of Selective Catalytic Reduction of NO_x by NH₃ over Cu-Exchanged SAPO-34. *ACS Catal.* **2013**, *3*, 871–881.
- (9) Akah, A. C.; Nkeng, G.; Garforth, A. A. The Role of Al and Strong Acidity in the Selective Catalytic Oxidation of NH₃ over Fe-ZSM-5. *Appl. Catal., B* **2007**, *74*, 34–39.
- (10) Long, R. Q.; Yang, R. T. Superior Ion-Exchanged ZSM-5 Catalysts for Selective Catalytic Oxidation of Ammonia to Nitrogen. *Chem. Commun.* **2000**, 1651–1652.
- (11) Li, P.; Zhang, R.; Liu, N.; Royer, S. Efficiency of Cu and Pd Substitution in Fe-Based Perovskites to Promote N₂ Formation during NH₃ Selective Catalytic Oxidation (NH₃-SCO). *Appl. Catal., B* **2017**, *203*, 174–188.
- (12) Kröcher, O.; Devadas, M.; Elsener, M.; Wokaun, A.; Söger, N.; Pfeifer, M.; Demel, Y.; Mussmann, L. Investigation of the Selective Catalytic Reduction of NO by NH₃ on Fe-ZSM5 Monolith Catalysts. *Appl. Catal., B* **2006**, *66*, 208–216.
- (13) Li, Y.; Armor, J. N. Selective NH₃ Oxidation to N₂ in a Wet Stream. *Appl. Catal., B* **1997**, *13*, 131–139.
- (14) Zhang, Q.; Zhang, T.; Xia, F.; Zhang, Y.; Wang, H.; Ning, P. Promoting Effects of Acid Enhancing on N₂ Selectivity for Selectivity Catalytic Oxidation of NH₃ over RuO_x/TiO₂: The Mechanism Study. *Appl. Surf. Sci.* **2020**, *500*, No. 144044.
- (15) Long, R. Q.; Yang, R. T. Noble Metal (Pt, Rh, Pd) Promoted Fe-ZSM-5 for Selective Catalytic Oxidation of Ammonia to N₂ at Low Temperatures. *Catal. Lett.* **2002**, *78*, 353–357.
- (16) Gang, L.; Anderson, B. G.; van Grondelle, J.; van Santen, R. A. Intermediate Species and Reaction Pathways for the Oxidation of Ammonia on Powdered Catalysts. *J. Catal.* **2001**, *199*, 107–114.
- (17) van de Water, L. G. A.; Bezemer, G. L.; Bergwerff, J. A.; Versluijs-Helder, M.; Weckhuysen, B. M.; de Jong, K. P. Spatially Resolved UV–Vis Microspectroscopy on the Preparation of Alumina-Supported Co Fischer–Tropsch Catalysts: Linking Activity to Co Distribution and Speciation. *J. Catal.* **2006**, *242*, 287–298.
- (18) Rout, K. R.; Baidoo, M. F.; Fenes, E.; Zhu, J.; Fuglerud, T.; Chen, D. Understanding of Potassium Promoter Effects on Oxychlorination of Ethylene by Operando Spatial-Time Resolved UV–Vis–NIR Spectrometry. *J. Catal.* **2017**, *352*, 218–228.
- (19) Urakawa, A.; Maeda, N.; Baiker, A. Space- and Time-Resolved Combined DRIFT and Raman Spectroscopy: Monitoring Dynamic Surface and Bulk Processes during NO_x Storage Reduction. *Angew. Chem., Int. Ed.* **2008**, *47*, 9256–9259.
- (20) Korup, O.; Goldsmith, C. F.; Weinberg, G.; Geske, M.; Kandemir, T.; Schlögl, R.; Horn, R. Catalytic Partial Oxidation of Methane on Platinum Investigated by Spatial Reactor Profiles, Spatially Resolved Spectroscopy, and Microkinetic Modeling. *J. Catal.* **2013**, *297*, 1–16.
- (21) Urakawa, A.; Trachsler, F.; von Rohr, P. R.; Baiker, A. On-Chip Raman Analysis of Heterogeneous Catalytic Reaction in Supercritical CO₂: Phase Behaviour Monitoring and Activity Profiling. *Analyst* **2008**, *133*, 1352–1354.
- (22) Grunwaldt, J.-D.; Kimmerle, B.; Baiker, A.; Boye, P.; Schroer, C. G.; Glatzel, P.; Borca, C. N.; Beckmann, F. Catalysts at Work: From Integral to Spatially Resolved X-Ray Absorption Spectroscopy. *Catal. Today* **2009**, *145*, 267–278.
- (23) Schroer, C. G.; Grunwaldt, J.-D. Spatially Resolved X-Ray Absorption Spectroscopy. *In-Situ Charact. Heterog. Catal.* **2013**, 49–73.
- (24) Dann, E. K.; Gibson, E. K.; Catlow, R. A.; Collier, P.; Erlep, Erden, T.; Gianolio, D.; Hardacre, C.; Kroner, A.; Raj, A.; Goguet, A.; Wells, P. P. Combined In Situ XAFS/DRIFTS Studies of the Evolution of Nanoparticle Structures from Molecular Precursors. *Chem. Mater.* **2017**, *29*, 7515–7523.
- (25) Russell, A.; Epling, W. S.; Hess, H.; Chen, H.-Y.; Henry, C.; Currier, N.; Yezerets, A. Spatially-Resolved Temperature and Gas Species Changes in a Lean-Burn Engine Emissions Control Catalyst. *Ind. Eng. Chem. Res.* **2010**, *49*, 10311–10322.
- (26) Goguet, A.; Stewart, C.; Toutou, J.; Morgan, K. Chapter Three - In Situ Spatially Resolved Techniques for the Investigation of Packed Bed Catalytic Reactors: Current Status and Future Outlook of Spaci-FB. In *Spatially Resolved Operando Measurements in Heterogeneous Catalytic Reactors*; Dixon, A. G.; Deutschmann, O.; Marin, G., Eds.; Academic Press, 2017; Vol. 50, pp 131–160.
- (27) Toutou, J.; Aiouache, F.; Burch, R.; Douglas, R.; Hardacre, C.; Morgan, K.; Sá, J.; Stewart, C.; Stewart, J.; Goguet, A. Evaluation of an in Situ Spatial Resolution Instrument for Fixed Beds through the Assessment of the Invasiveness of Probes and a Comparison with a Micro-Kinetic Model. *J. Catal.* **2014**, *319*, 239–246.
- (28) Nachtegaal, M.; Müller, O.; König, C.; Frahm, R. QEXAFS: Techniques and Scientific Applications for Time-Resolved XAS. In *X-Ray Absorption and X-Ray Emission Spectroscopy*; John Wiley & Sons, Ltd, 2016; pp 155–183.
- (29) Clark, A. H.; Imbao, J.; Frahm, R.; Nachtegaal, M. ProQEXAFS: A Highly Optimized Parallelized Rapid Processing Software for QEXAFS Data. *J. Synchrotron Radiat.* **2020**, *27*, 551–557.
- (30) Ravel, B.; Newville, M. Athena, Artemis, Hephaestus: Data Analysis for x-Ray Absorption Spectroscopy Using IFEFFIT. *J. Synchrotron Radiat.* **2005**, *12*, 537.
- (31) Newville, M. IFEFFIT: Interactive XAFS Analysis and FEFF Fitting. *J. Synchrotron Radiat.* **2001**, *8*, 322.
- (32) Voronov, A.; Urakawa, A.; Beek, W.; van Tsakoumis, N. E.; Emerich, H.; Rønning, M. Multivariate Curve Resolution Applied to in Situ X-Ray Absorption Spectroscopy Data: An Efficient Tool for Data Processing and Analysis. *Anal. Chim. Acta* **2014**, *840*, 20–27.
- (33) Cassinelli, W. H.; Martins, L.; Passos, A. R.; Pulcinelli, S. H.; Santilli, C. V.; Rochet, A.; Briois, V. Multivariate Curve Resolution Analysis Applied to Time-Resolved Synchrotron X-Ray Absorption Spectroscopy Monitoring of the Activation of Copper Alumina Catalyst. *Catal. Today* **2014**, *229*, 114–122.
- (34) Clark, A. H.; Nuguid, R. J. G.; Steiger, P.; Marberger, A.; Petrov, A. W.; Ferri, D.; Nachtegaal, M.; Kröcher, O. Selective Catalytic Reduction of NO with NH₃ on Cu–SSZ-13: Deciphering

the Low and High-Temperature Rate-Limiting Steps by Transient XAS Experiments. *ChemCatChem* **2020**, *12*, 1429–1435.

(35) Olmos, V.; Benítez, L.; Marro, M.; Loza-Alvarez, P.; Piña, B.; Tauler, R.; de Juan, A. Relevant Aspects of Unmixing/Resolution Analysis for the Interpretation of Biological Vibrational Hyperspectral Images. *TrAC, Trends Anal. Chem.* **2017**, *94*, 130–140.

(36) Rochet, A.; Baubet, B.; Moizan, V.; Pichon, C.; Briois, V. Co-K and Mo-K Edges Quick-XAS Study of the Sulphidation Properties of Mo/Al₂O₃ and CoMo/Al₂O₃ Catalysts. *C. R. Chim.* **2016**, *19*, 1337–1351.

(37) Ruckebusch, C.; Blanchet, L. Multivariate Curve Resolution: A Review of Advanced and Tailored Applications and Challenges. *Anal. Chim. Acta* **2013**, *765*, 28–36.

(38) Windig, W.; Stephenson, D. A. Self-Modeling Mixture Analysis of Second-Derivative near-Infrared Spectral Data Using the SIMPLISMA Approach. *Anal. Chem.* **1992**, *64*, 2735–2742.

(39) Tauler, R.; Lacorte, S.; Barceló, D. Application of Multivariate Self-Modeling Curve Resolution to the Quantitation of Trace Levels of Organophosphorus Pesticides in Natural Waters from Interlaboratory Studies. *J. Chromatogr. A* **1996**, *730*, 177–183.

(40) Decarolis, D.; Lezcano-Gonzalez, I.; Gianolio, D.; Beale, A. M. Effect of Particle Size and Support Type on Pd Catalysts for 1,3-Butadiene Hydrogenation. *Top. Catal.* **2018**, 162–174.

(41) Srabionyan, V. V.; Bugaev, A. L.; Pryadchenko, V. V.; Avakyan, L. A.; van Bokhoven, J. A.; Bugaev, L. A. EXAFS Study of Size Dependence of Atomic Structure in Palladium Nanoparticles. *J. Phys. Chem. Solids* **2014**, *75*, 470–476.

(42) Bahruji, H.; Bowker, M.; Hutchings, G.; Dimitratos, N.; Wells, P.; Gibson, E.; Jones, W.; Brookes, C.; Morgan, D.; Lalev, G. Pd/ZnO Catalysts for Direct CO₂ Hydrogenation to Methanol. *J. Catal.* **2016**, *343*, 133–146.

(43) Beale, A. M.; Weckhuysen, B. M. EXAFS as a Tool to Interrogate the Size and Shape of Mono and Bimetallic Catalyst Nanoparticles. *Phys. Chem. Chem. Phys.* **2010**, *12*, 5562–5574.

(44) Bugaev, A. L.; Usoltsev, O. A.; Guda, A. A.; Lomachenko, K. A.; Pankin, I. A.; Rusalev, Y. V.; Emerich, H.; Groppo, E.; Pellegrini, R.; Soldatov, A. V.; van Bokhoven, J. A.; Lamberti, C. Palladium Carbide and Hydride Formation in the Bulk and at the Surface of Palladium Nanoparticles. *J. Phys. Chem. C* **2018**, *122*, 12029–12037.

(45) Chan, C. W. A.; Mahadi, A. H.; Li, M. M.-J.; Corbos, E. C.; Tang, C.; Jones, G.; Kuo, W. C. H.; Cookson, J.; Brown, C. M.; Bishop, P. T.; Tsang, S. C. E. Interstitial Modification of Palladium Nanoparticles with Boron Atoms as a Green Catalyst for Selective Hydrogenation. *Nat. Commun.* **2014**, *5*, No. 5787.

(46) Wang, L.; Yin, C.; Yang, R. T. Selective Catalytic Reduction of Nitric Oxide with Hydrogen on Supported Pd: Enhancement by Hydrogen Spillover. *Appl. Catal., A* **2016**, *514*, 35–42.

(47) Qi, G.; Yang, R. T.; Rinaldi, F. C. Selective Catalytic Reduction of Nitric Oxide with Hydrogen over Pd-Based Catalysts. *J. Catal.* **2006**, *237*, 381–392.

(48) Ohtsuka, H.; Tabata, T.; Hirano, T. Palladium–Platinum-Loaded Sulfated Zirconia: A Highly Durable Catalyst for the Reduction of Nitrogen Oxides by Methane in the Presence of Water Vapor and SO_x. *Appl. Catal., B* **2000**, *28*, L73–L76.

(49) Ohtsuka, H.; Tabata, T. Roles of Palladium and Platinum in the Selective Catalytic Reduction of Nitrogen Oxides by Methane on Palladium–Platinum-Loaded Sulfated Zirconia. *Appl. Catal., B* **2001**, *29*, 177–183.